Chemical Science

ROYAL SOCIETY OF CHEMISTRY

EDGE ARTICLE

View Article Online
View Journal

Cite this: DOI: 10.1039/d5sc09647b

All publication charges for this article have been paid for by the Royal Society of Chemistry

The critical role of isolated Ti^{3+} sites in MIL-125 for photocatalytic nitrate reduction: performance enhancement and deactivation mechanism

Lijun Liao, *[ac] Guangquan Zhao,[b] Ruiwen Shu,*[ad] Xuepeng Wang, [b] Jinxin Zhang[a] and Ruting Yuan*[b]

Received 9th December 2025
Accepted 20th February 2026

DOI: 10.1039/d5sc09647b

rsc.li/chemical-science

Photocatalytic reduction of nitrate (NO_3^-) to ammonia (NH_3) represents a sustainable route for wastewater treatment and chemical production. Metal–organic frameworks (MOFs) such as MIL-125 are promising catalysts, yet their performance often decays during reaction. This study reveals that the aggregation state of Ti^{3+} sites in MIL-125 is a critical factor governing its photocatalytic efficiency. We demonstrate that the as-synthesized MIL-125, featuring isolated Ti^{3+} sites, achieves a high NH_3 production rate of 738.32 μmol g^{-1} h^{-1} under full-spectrum light without sacrificial agents. Comprehensive characterization and theoretical calculations indicate that these isolated Ti^{3+} sites elevate the material's conduction band and enhance NO_3^- adsorption, thereby lowering the energy barrier for the rate-determining step. However, prolonged photoreaction leads to linker deficiency, resulting in agglomeration of Ti^{3+} sites. This structural evolution causes a negative shift in the conduction band potential, impedes charge separation, and increases the reaction barrier, leading to a noticeable loss in activity over cycles. This work underscores the pivotal role of maintaining isolated metal sites for designing stable and efficient MOF-based photocatalysts for nitrogen cycling.

1 Introduction

Ammonia (NH_3) is an indispensable chemical widely used in agricultural fertilizers and is considered a promising carbon-free energy carrier due to its high hydrogen density.[1,2] Currently, NH_3 is predominantly synthesized *via* the Haber–Bosch process, which operates under severe conditions of high temperature (400–500 °C) and pressure (150–300 atm), consuming 1.0–2.0% of the world's energy supply and accounting for approximately 1.6% of global carbon emissions.[3,4] The extreme energy demands are primarily due to the high dissociation energy (941 kJ mol^{-1}) of the inert N≡N bond in dinitrogen (N_2) and its low solubility in aqueous systems, thereby posing significant kinetic challenges.[5,6] Photocatalytic nitrate (NO_3^-) reduction for ammonia synthesis under ambient conditions may serve as a complementary approach rather than a direct replacement for the Haber–Bosch process in large-scale industrial settings. This route is advantageous because the N=O bond in NO_3^- has a lower dissociation energy (204 kJ mol^{-1}), and nitrate is highly soluble in water and abundantly present as a pollutant in wastewater.[7,8] The overall reaction ($NO_3^- + 9H^+ + 8e^- \rightarrow NH_3 + 3H_2O$) offers a pathway for simultaneous wastewater treatment and value-added ammonia synthesis under ambient conditions.[9]

Photocatalytic NH_3 production from NO_3^- reduction is a promising strategy for simultaneous wastewater treatment and sustainable NH_3 synthesis. The efficiency of this process is primarily governed by the catalyst's ability to adsorb NO_3^-, multi-electron transfer efficiency, and reaction energy barriers.[10] Recent advancements focus on sophisticated material design to optimize these steps. Defect engineering, such as introducing boron dopants and nitrogen vacancies into g-C_3N_4, can modulate the electronic structure to strengthen nitrate adsorption and inhibit hydrogen evolution, thereby achieving high photocatalytic performance for NH_3 generation.[11] The construction of $Ta_3N_5/CdIn_2S_4$ S-scheme heterojunctions can promote efficient charge separation while preserving strong redox potentials, which is crucial for the demanding 8-electron reduction process.[12] In addition, the incorporation of single-atom catalysts, such as Ni on defective WO_3 or Pt on Ti-deficient TiO_2 nanosheets, provides highly active sites that not only lower the energy barriers for key reaction steps but also enhance selectivity by minimizing undesirable N_2 formation.[13,14] Moreover, strategies like coupling the reduction reaction with the oxidation of sacrificial agents such as formic acid can generate

[a]School of Chemical and Blasting Engineering, School of Earth and Environment, Anhui University of Science and Technology, Huainan, 232001, China. E-mail: lijun.liao@aust.edu.cn; rwshu@aust.edu.cn

[b]School of Chemistry and Chemical Engineering, Qilu University of Technology (Shandong Academy of Sciences), Jinan, Shandong, 250353, China. E-mail: rutingyuan@qlu.edu.cn

[c]Hubei Key Laboratory of Novel Reactor and Green Chemical Technology, Wuhan Institute of Technology, Wuhan 430072, China

[d]State Key Laboratory of New Textile Materials and Advanced Processing, Wuhan Textile University, Wuhan 430200, China

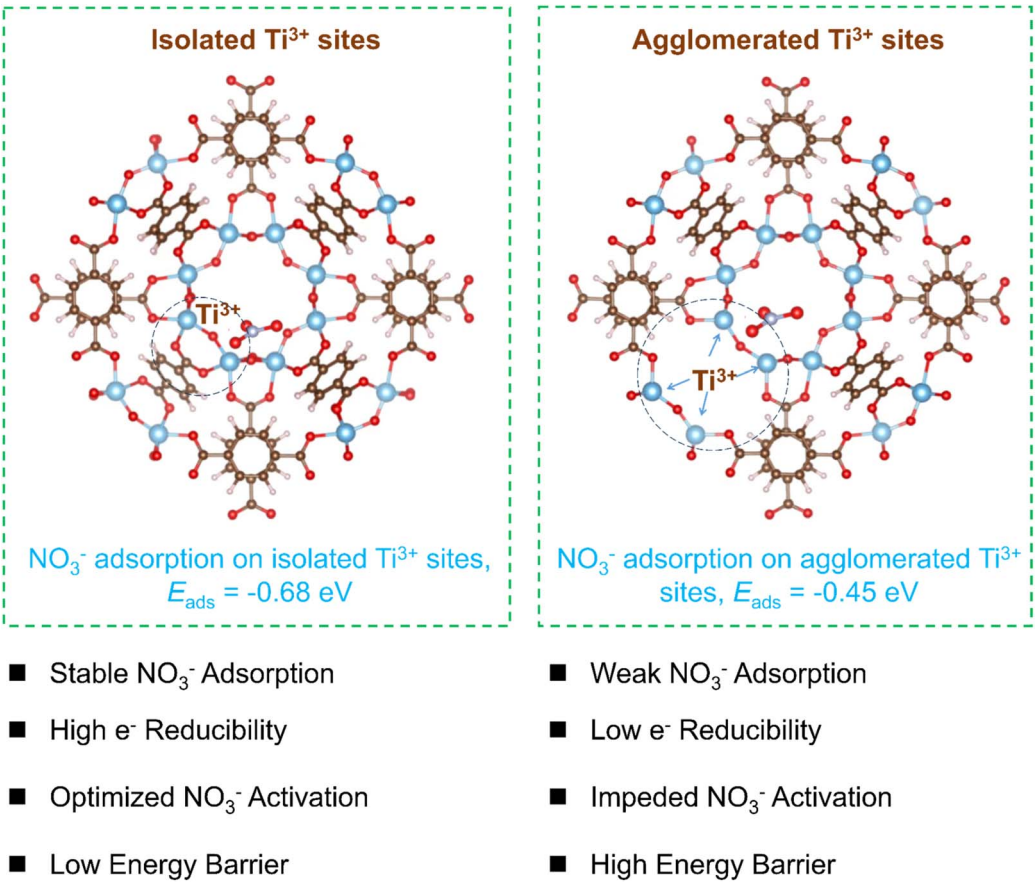

Fig. 1 The presence of isolated Ti^{3+} sites (left) in MIL-125 shifts the d-band center upward relative to the Fermi level of Ti sites in comparison with agglomerated Ti^{3+} sites (right), leading to enhanced NO_3^- adsorption and higher reduction potential, thereby optimizing NO_3^- activation and lowering the energy barrier for NH_3 generation.

additional reducing radicals such as $CO_2^{\bullet-}$, which synergistically enhance the overall reduction efficiency.[15]

Metal–organic frameworks (MOFs) are promising photocatalysts for NH_3 production *via* NO_3^- reduction, owing to their structural tunability, which enhances catalytic activity.[16,17] Doping Ru into a Ni-MOF can shift the d-band center of adjacent Ni sites, thereby optimizing the adsorption strength of nitrogen intermediates and boosting catalytic performance.[18] Similarly, incorporating Cu^{2+} into NH_2-MIL-125 can induces p–d orbital hybridization between Cu 3d and nitrate O 2p orbitals, thereby stabilizing bidentate nitrate adsorption and lowering the activation energy barrier for a high NH_3 yield of 32.8 mg g^{-1} h^{-1}.[19] Another prominent strategy involves constructing nanoarchitectured heterojunctions, such as the S-scheme system in NH_2-MIL-125@Co(OH)$_2$ confined within a ZIF-8 "nanohouse", which improves electron–hole separation and utilizes the ZIF-8 shell's positive charge to enrich nitrate reactants and suppress competing hydrogen evolution, thus achieving a high NH_3 yield of 2454.9 μmol g^{-1} h^{-1}.[20] These studies demonstrate that rational design of MOF-based photocatalysts is a highly effective route for efficient photocatalytic NH_3 synthesis. Structural defects in MOFs, whether intrinsically formed or deliberately engineered to enhance catalytic properties, are frequently implicated in performance decay under practical operating conditions. Defect sites, such as missing linkers or clusters, can act as preferential adsorption centers for poisons, leading to site blocking and reduced catalytic activity, as demonstrated in NH_3-SCR systems for NO_x abatement where poisoning accelerates deactivation.[21] Moreover, defects can lower the thermal and chemical stability of MOFs, promoting sintering of metal nodes, phase transformations, or framework collapse, which irreversibly diminishes catalytic efficiency over time.[22] For instance, in thermally defect-engineered precious group MOFs such as Ru/Rh-HKUST-1, while the initial activity may be enhanced, uncontrolled defect generation can introduce unstable, reduced metal sites that facilitate unwanted side reactions or structural degradation, ultimately leading to catalyst deactivation.[23] A critical balance in defect density and characterization is essential to harness benefits while mitigating performance decay. However, to our knowledge, the influence of the change in the Ti^{3+} site induced by surface reconstruction and defect generation during the reaction on NH_3 photosynthesis efficiency has never been reported.

In this study, we demonstrate the presence of isolated Ti^{3+} sites in as-prepared MIL-125 to enhance NO_3^- adsorption and generate high-energy electrons, lowering reaction energy barriers and promoting NH_3 photosynthesis efficiency (Fig. 1 left). However, agglomerated Ti^{3+} sites can form during

photocatalytic nitrate reduction due to increased missing linkers in MIL-125 (Fig. 1, right), thereby decreasing catalytic performance. Theoretical and experimental results show that isolated Ti^{3+} sites in MIL-125 increase the electron density and the conduction band minimum, thereby enhancing NO_3^- adsorption and photo-induced electron reduction capacity. The highest NH_3 photosynthesis rate of 738.32 μmol g_{cat}^{-1} h^{-1} can be achieved in the absence of a sacrificial agent under full-spectrum illumination.

2 Materials and methods

Commercial reagents were utilized in this work, including terephthalic acid (TPA), *N*,*N*-dimethylformamide (DMF), tetra-*n*-butyl titanate ($Ti(OC_4H_9)_4$), and methanol (CH_3OH), which were purchased from Shanghai Aladdin Biochemical Technology Co., Ltd. Terephthalic acid (3 g, 18 mmol) was dissolved in 54 mL of *N*,*N*-dimethylformamide (DMF) and stirred for 30 min until complete dissolution. Meanwhile, tetra-*n*-butyl titanate $Ti(OC_4H_9)_4$ (1.56 mL, 4.5 mmol) was added dropwise to 6 mL of methanol and stirred for 30 min to form a transparent solution. Then, the latter solution containing the titanate was slowly added to the former solution containing the organic linker. The color of the mixture slowly changed from pale yellow to milky white under continuous stirring for 30 min. The mixture was afterwards heated in an oil bath at 100 °C for 24 h under reflux. After cooling to room temperature, the suspension was centrifuged at 6000 rpm for 3 min and then washed with 25 mL DMF to remove the unreacted organic ligands. Afterwards, the collected white MIL-125 powder was washed with 25 mL methanol three times and dried at 80 °C in an oven overnight. Characterization and photocatalytic nitrate reduction reaction with specific details are described in the SI.

3 Results and discussion

3.1 NO_3^- to NH_4^+ photosynthesis performance

The evaluation of NO_3^- reduction for NH_4^+ photosynthesis was first performed in a 50 mL $NaNO_3$ solution (2 g L^{-1} of NO_3^-) without any sacrificial agents under full-spectrum illumination. Generally, 25 mg of as-prepared MIL-125 was employed as the photocatalyst in the reaction system, above which light illumination was applied. As depicted in Fig. 2a, the as-made MIL-125 exhibits excellent photocatalytic performance for NO_3^- reduction to NH_4^+, achieving a NH_4^+ photosynthesis rate of 738.32 μmol g_{cat}^{-1} h^{-1}. The control experiments were conducted by omitting NO_3^- or MIL-125 from the reaction system. The reaction mixture was illuminated for 1 h and sampled every 15 min. Ultrapure water (18.2 MΩ cm) and high-purity $NaNO_3$ (>99%) were utilized during the photocatalytic reactions to exclude potential ammonia contamination. Direct analysis of $NaNO_3$ solution by Nessler's reagent method was conducted, thereby confirming the absence of ammonia in the prepared solutions. It is observed that no NH_4^+ was formed under light illumination without NO_3^- or MIL-125 (Fig. 2a). In addition, no NH_4^+ was detected in the catalysis system of MIL-125 in the absence of light illumination, indicating that the NO_3^- reduction to NH_4^+ process was driven by photocatalysis. Since the photocatalytic efficiency is directly influenced by reaction parameters, the reaction parameters, including photocatalyst dosage (Fig. 2b), light source (Fig. 2c), and nitrate concentration (Fig. 2d) are thoroughly investigated to further enhance photocatalytic activity for ammonia synthesis from nitrate reduction. As presented in Fig. 2b, the optimized photocatalyst dosage was 25 mg to achieve the highest photocatalytic activity for NO_3^- reduction to NH_4^+. In addition, due to the low UV content in solar energy, various light sources were used to evaluate photocatalytic performance, as shown in Fig. 2c. The optimal NH_4^+ formation efficiency with MIL-125 is achieved under full-spectrum light illumination.

The nitrate concentration was optimized to enhance photocatalytic performance, as demonstrated in Fig. 2d. It is observed that the relative increase in nitrate concentration improves the reaction kinetics of the photocatalytic nitrate reduction reaction, thereby enhancing photocatalytic activity. Notably, during all conducted experiments, MIL-125 demonstrated slightly decreased photocatalytic activity for the NH_4^+ synthesis rate. Therefore, long-term recyclability measurements were further investigated for NH_4^+ production *via* NO_3^- reduction (Fig. 2e). Similarly, the MIL-125 nanoparticles exhibit a significant decrease in photocatalytic performance after 5 consecutive cycles. As shown in Fig. 2e, the NH_4^+ photosynthesis rate decreased from 738.32 to 612.82 μmol g_{cat}^{-1} h^{-1} after recyclability measurements probably due to structural defects created during the reaction process, which will be discussed in subsequent sections. Although MIL-125 presented decreased activity for NH_4^+ photosynthesis, comparative analyses with other photocatalysts suggest that the as-prepared MIL-125 achieved a decent photocatalytic activity for nitrated reduction without a sacrificial agent and cocatalyst, as shown in Fig. 2f and Table S1 (SI).

3.2 Characterization and electronic properties of MIL-125 before and after the reaction

Since the photocatalytic performance of MIL-125 in the nitrate reduction reaction decreased with reaction time, various characterization studies of the sample before and after the reaction were conducted to unravel the mystery of this phenomenon. The crystal structures of the freshly prepared MIL-125 and the sample after a 1 h photocatalytic NO_3^- reduction reaction were examined by XRD. As revealed in Fig. 3a, the XRD patterns of MIL-125 after the 1 h reaction did not demonstrate compelling differences compared to the pristine MIL-125 before the reaction, suggesting that the main phase structure of MIL-125 was retained after the photocatalytic nitrate reduction reaction.[24] The SEM image of MIL-125 (Fig. 3b) reveals a cake-like morphology with random pores. Notably, after 1 h of photocatalytic nitrate reduction, the sample demonstrated a similar morphology with a rough surface, as shown in Fig. 3c. This result indicates that certain surface reconstruction occurred on MIL-125 during the nitrate photo–reduction reaction, although the crystal structure of the sample was maintained after the reaction. A closer observation of the TEM images (Fig. 3d–f) shows that the diameter of the MIL-125 nanoparticles is around

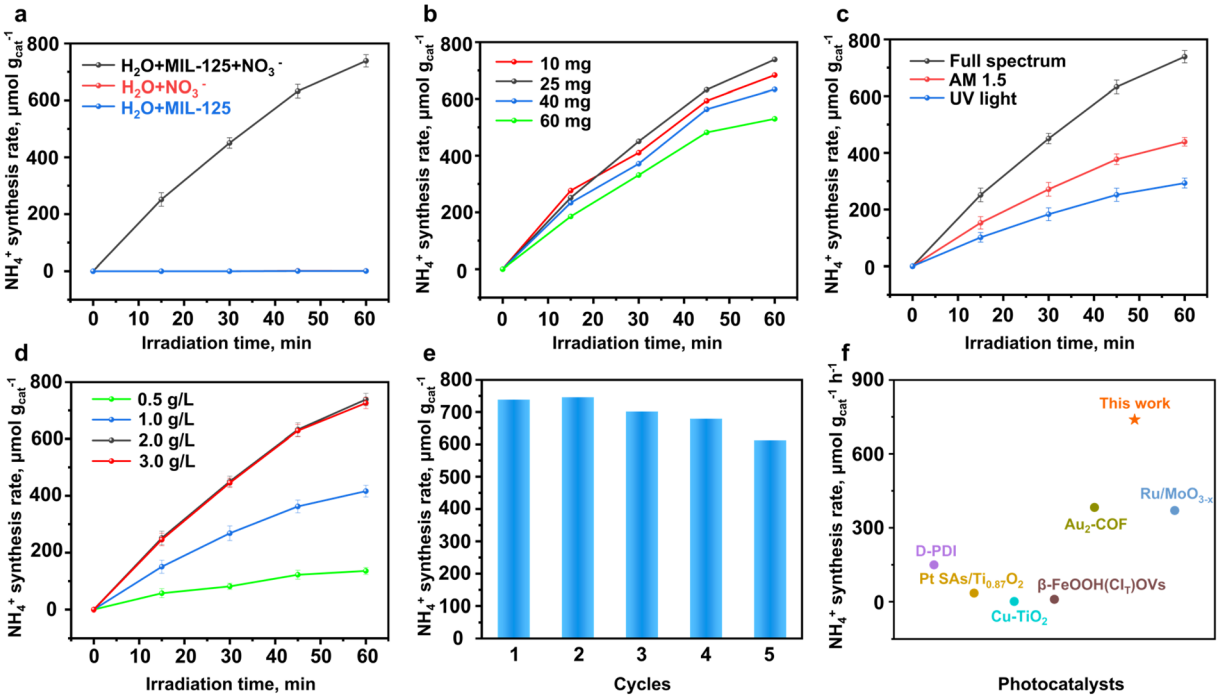

Fig. 2 (a) Control experiment conducted without NO_3^- or MIL-125 in the reaction system (duration: 60 min; sampled every 15 min; detected by Nessler's reagent method). Photocatalyst dosage optimization (b), light source optimization (c), and initial NO_3^- concentration optimization (d) on MIL-125 for the promotion of NH_4^+ formation efficiency. (e) NH_4^+ photosynthesis rate during the recycling stability test. (f) Comparison of NH_4^+ photosynthesis rate with previously reported photocatalysts.

400 nm. Fig. 3g–i shows that the MIL-125 sample after the reaction demonstrated similar particle sizes and morphology. Compared with the pristine MIL-125, the sample after the reaction also shows surface roughness, as observed in the TEM images (Fig. 3g–i). In addition, more pores can be observed in the samples after photocatalytic nitrate reduction, suggesting that possible structural defects may have been generated during the reaction.

To investigate the porosity of MIL-125 before and after the reaction, the BET surface area and pore size distribution were analyzed from the N_2 sorption isotherm. As shown in Fig. 4a, both samples exhibit type IV N_2 sorption isotherm curves with an untypical hysteresis loop,[25] suggesting the existence of hierarchical porous structures.[26] The N_2 isotherm curve of the pristine MIL-125 shows significant adsorption at a low relative pressure (P/P_0 below 0.01) before reaching a plateau, confirming the presence of large amounts of micropores in the sample.[27] In contrast, after 1 h of nitrate reduction reaction, only a slight increase in the adsorption isotherm at a relatively low pressure can be observed, indicating that most micropores in the sample disappeared after the photocatalytic reaction. Notably, compared to the pristine MIL-125, the hysteresis loop is much more pronounced in the N_2 sorption isotherm of the sample after the photocatalytic nitrate reduction reaction, indicating that more mesopores were produced after the reaction. In addition, the BET surface area of MIL-125 decreased sharply from 1195 to 278 $m^2\ g^{-1}$ after the reaction, probably due to partial removal of the organic linkers, consistent with the N_2 adsorption isotherm results. The decreased surface area could provide fewer active sites and reduced mass transfer efficiency, thereby decreasing the photocatalytic activity. The pore size distributions also verify the generation of mesopores in the sample after the photocatalytic reaction, as presented in Fig. 4b.

To unravel the surface electronic structure and chemical state of the samples before and after the reaction, XPS measurements were performed (Fig. 4c–f). In the survey spectra, three dominant signals at 284, 458, and 531 eV can be ascribed to C 1s, Ti 2p, and O 1s, respectively, as shown in Fig. 4c. The C 1s XPS spectra in Fig. 4d confirm the presence of terephthalic acid in both samples. The XPS peaks at 284.28, 286.09, and 288.23 eV can be ascribed to C=C, C–O, and C=O bonds, respectively, in the organic ligands in MIL-125.[28] The binding energies at 458.37 and 464.18 eV in the Ti 2p XPS spectra can be attributed to Ti $2p_{3/2}$ and Ti $2p_{1/2}$ of the tetra-valent Ti^{4+} in the Ti-oxo clusters, respectively.[29] The XPS signals of tri-valence Ti^{3+} at the binding energies of 456.96 and 463.00 eV are observed in both pristine MIL-125 and the sample after the reaction, suggesting the presence of organic ligand defects in both samples.[30] A small amount (*ca.* 10%) of missing linker defects are typically present in MOFs synthesized by a regular process[31] Notably, the ratios of Ti^{3+} in the as-prepared MIL-125 obviously increased after the photocatalytic nitrate reduction reaction due to the increased missing ligands, thereby resulting in the agglomeration of the active Ti^{3+} sites. In addition, the binding energy of Ti^{3+} in the sample after the reaction shifted to a higher energy by 0.18 eV, which may be due to electron delocalization among agglomerated Ti^{3+} sites, resulting in a decrease in the electron cloud density around Ti^{3+}.[29] This result could lead to

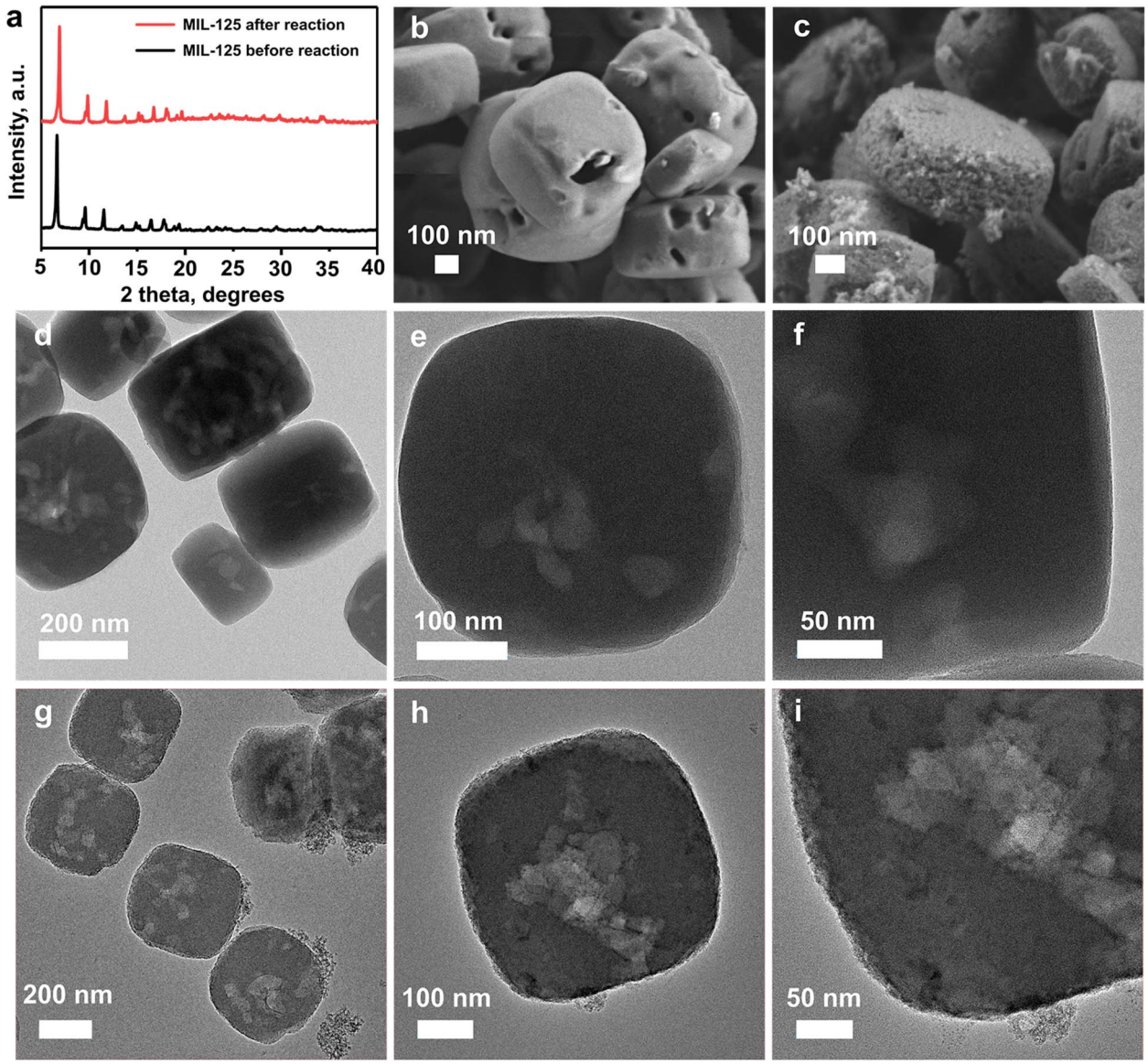

Fig. 3 Crystal structure and the morphology characterization for MIL-125 before and after the 1 h reaction. (a) Powder XRD profiles of the freshly prepared MIL-125 sample and the one after 1 h photocatalytic NO_3^- reduction. (b) SEM image of the freshly prepared MIL-125 sample. (c) SEM image of the MIL-125 sample after 1 h photocatalytic NO_3^- reduction. (d–f) High-resolution TEM images of the freshly prepared MIL-125 sample. (g–i) High resolution TEM images of the MIL-125 sample after 1 h photocatalytic NO_3^- reduction.

a decreased reduction capacity of the Ti^{3+} sites, thereby undermining the photocatalytic activity for nitrate reduction. In the O 1s XPS spectra (Fig. 4f), three binding energies centred at 530.20, 531.74, and 533.18 eV can be attributed to Ti–O, C=O, and hydroxyl groups, respectively.[29] It can be observed that the ratio of C=O significantly decreased in the used sample due to the removal of organic ligands in MIL-125.

3.3 Investigation of the reaction mechanism

The optical properties of the samples were analyzed using solid-state UV-vis DRS. A redshift of the light absorption edge of MIL-125 was observed in Fig. 4g due to the formation of structural defects. The bandgap energy of the samples before and after the reaction was determined by the Tauc plot to be 3.54 and 3.21 eV, respectively (Fig. 4h). Although the light-utilizing ability of the sample after the reaction was improved, the photocatalytic performance for nitrate reduction gradually decreased (Fig. 2a–e). This phenomenon can be explained by the fact that photocatalytic activity is not only determined by light utilization but also by the reducibility of photo-generated electrons, reactant adsorption, and the reaction energy barrier at the rate-determining step. As mentioned before, the increased linker defects induced aggregated Ti^{3+} sites, thereby changing the band structures, lowering the reduction potential, and weakening nitrate adsorption possibly due to the downward d-band center shift.[32] Mott–Schottky plots of the MIL-125 samples (Fig. 4i and S1 in the SI) before and after the reaction were utilized to determine the corresponding band structures. Positive slopes were identified in the Mott–Schottky plots, suggesting the n-

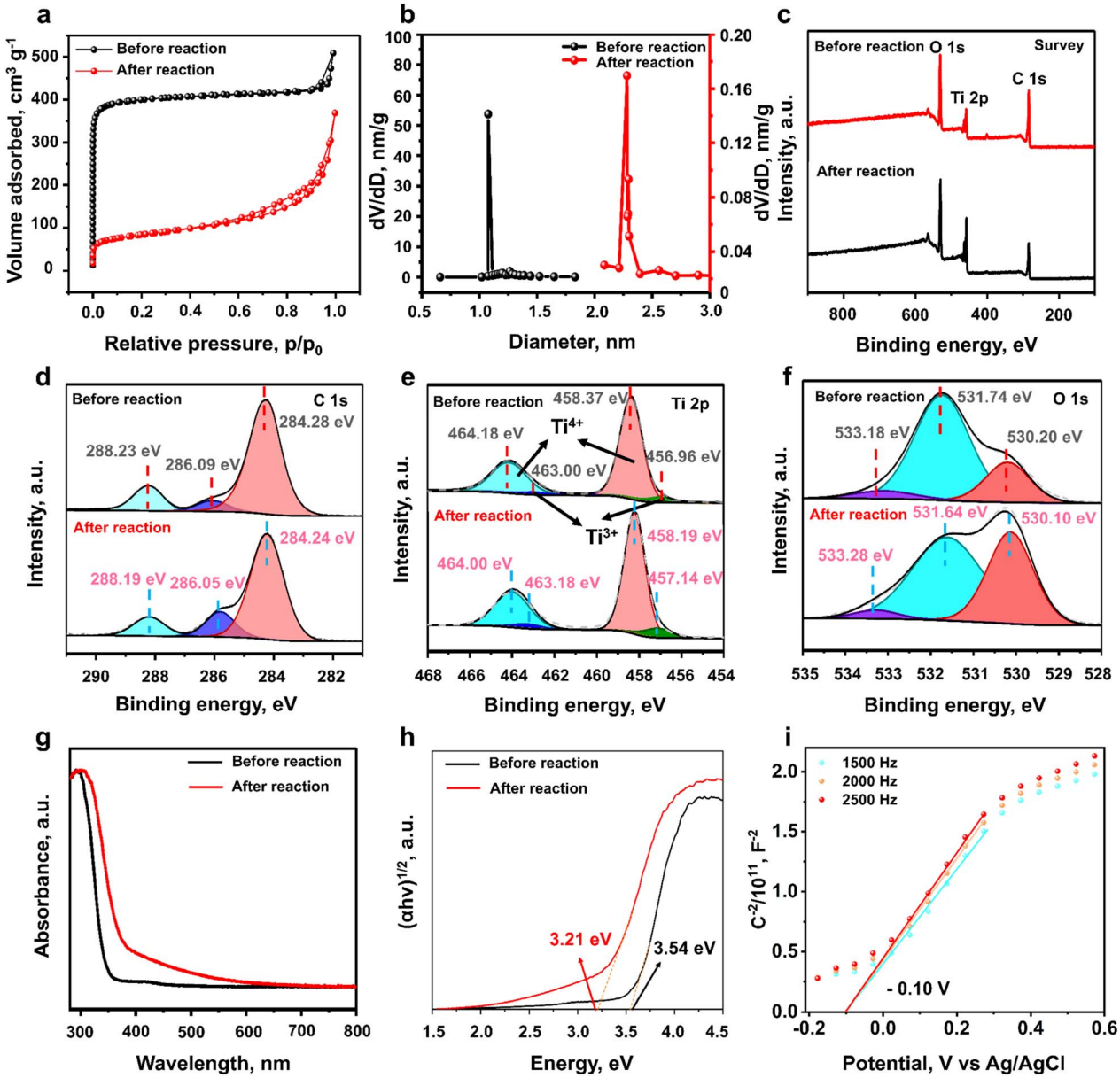

Fig. 4 Chemical and optical properties of MIL-125 before and after the reaction. (a) N_2 sorption isotherm, (b) pore size distributions, (c) XPS survey spectra, (d) C 1s, (e) Ti 2p, and (f) O 1s high-resolution XPS spectra, (g) UV-vis DRS, (h) Tauc plots of the freshly prepared MIL-125 sample and the one after 1 h photocatalytic NO_3^- reduction, and (i) Mott–Schottky curves of the pristine MIL-125.

type nature of the MIL-125 photocatalyst.[33] The flat band potentials of pristine MIL-125 and the one after the reaction were determined to be −0.10 and −0.04 V, respectively. In n-type semiconductors, the conduction band typically showed a more negative potential, around −0.10 V, relative to the corresponding flat band potential.[34] Therefore, the conduction band minima of pristine MIL-125 and the one after the reaction can be calculated to be −0.20 and −0.14 V, respectively.

Based on the above results and the obtained bandgap energies, the band structures of the samples are proposed in Fig. 5a. Both band alignments are suitable for nitrate reduction to ammonia (NO_3^-/NH_3, 1.20 V *vs.* NHE),[3] as presented in Fig. 5a. The conduction band edge (−0.20 V) of pristine MIL-125 with isolated Ti^{3+} sites is more negative than that (−0.14 V) of the sample after the reaction with agglomerated Ti^{3+} sites, indicating that the reducibility of photo-generated electrons decreased as the reaction proceeded due to the change of band alignment. To investigate the charge-separation efficiency of the samples, photoluminescence (PL) measurements were conducted with an excitation wavelength of 240 nm. As shown in Fig. 5b, the sample after the reaction exhibited much higher PL intensity than the original MIL-125, suggesting decreased charge separation and transfer efficiency.[35] The oxygen vacancies of MIL-125 before and after the reaction induced by the missing linkers were studied by EPR. As presented in Fig. 5c, the pristine MIL-125 exhibits an EPR signal at $g = 2.004$ in the spectrum, indicating that certain amounts of structural defects were present in the as-prepared original sample.[36] The sample

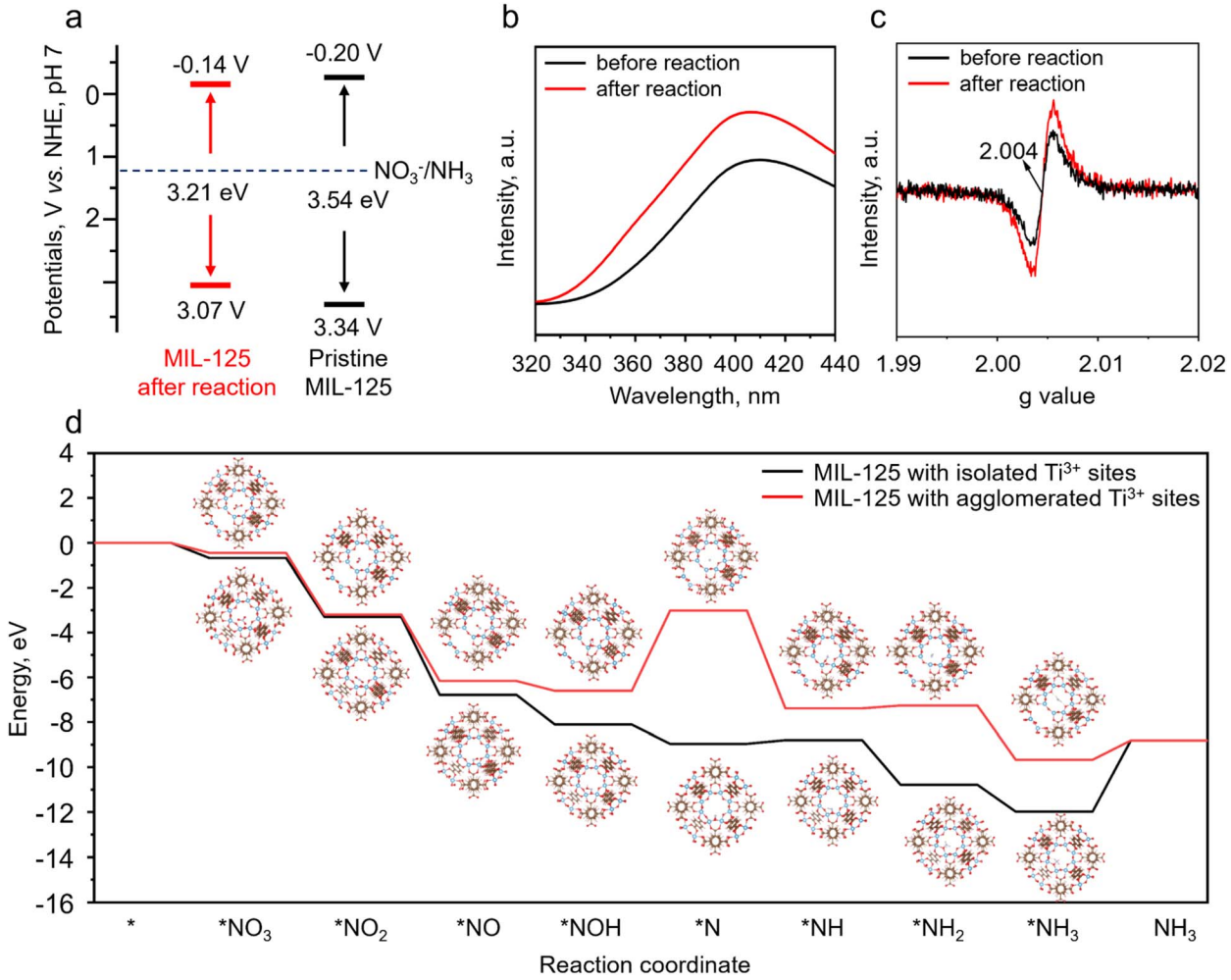

Fig. 5 (a) Band alignments, (b) PL spectra, and (c) EPR spectra of MIL-125 before and after the reaction. (d) Energy barriers from DFT calculations for the reduction of NO_3^- to NH_3 on MIL-125 with isolated Ti^{3+} sites and on MIL-125 with agglomerated Ti^{3+} sites.

after the photocatalytic nitrate reduction reaction presents higher EPR signal intensity than the original MIL-125, confirming that more oxygen vacancies were created because of the removal of organic ligands during the reaction process. This result is consistent with XPS and N_2 sorption isotherm results. Therefore, the XPS, EPR, and BET trends are consistent with the above-mentioned hypothesis that certain amounts of organic ligands were lost during the photocatalytic nitrate reduction process. Thermogravimetric analysis (TGA) was utilized to provide direct confirmation of ligand loss. As shown in Fig. S2 (SI), approximately 25% of the organic linkers lost during the photocatalytic nitrate reduction process,[37] which is consistent with the XPS, EPR, and BET results, providing direct evidence of the linker loss.

Based on the above investigations, fewer structural defects in pristine MIL-125 could induce the formation of isolated Ti^{3+} sites, as previously proposed in Fig. 1. Many more ligand defects formed during the photocatalytic nitrate reduction process could lead to the generation of agglomerated Ti^{3+} sites. Density functional theory (DFT) calculations were applied to further investigate the photocatalytic mechanism and rate-determining step in the NO_3^- reduction to NH_3 process. The energy barriers for elemental steps in the nitrate reduction to ammonia process in the presence of MIL-125 with isolated Ti^{3+} sites or agglomerated Ti^{3+} sites are presented in Fig. 5d. The adsorption energy of NO_3^- on MIL-125 with isolated Ti^{3+} sites (−0.68 eV) is obviously higher than that of MIL-125 with agglomerated Ti^{3+} sites (−0.45 eV), which could accelerate the nitrate reduction process. The rate-determining step in nitrate reduction in the presence of MIL-125 with agglomerated Ti^{3+} sites is the formation of *N from *NOH with a reaction energy barrier of 3.59 eV (Fig. 5d). With the presence of isolated Ti^{3+} sites in MIL-125, the rate-determining step in nitrate reduction to ammonia is the desorption of NH_3 with a lower reaction energy barrier of 3.17 eV. Although this barrier is reduced compared to the agglomerated case, it is by no means negligible and represents a significant kinetic limitation even for the optimized catalyst. The high desorption energy suggests that NH_3 release may inherently constrain the maximum achievable activity, underscoring that the initial high performance relies on the balanced enhancement of nitrate adsorption and charge separation to partially offset this limitation. Future study should be

conducted to decrease the large barrier for NH_3 desorption to further improve NH_3 photosynthesis efficiency. Nevertheless, the existence of isolated Ti^{3+} sites in MIL-125 could promote the nitrate adsorption and charge separation and transfer efficiency, and lower the reaction energy barrier for NH_3 photosynthesis. However, the increased amounts of missing ligands in MIL-125 during the nitrate reduction process induced agglomerated Ti^{3+} sites, thereby lowering the reducibility of photo-generated electrons, increasing the reaction energy barrier, and decreasing photocatalytic activity for NH_3 photosynthesis. The DFT calculations provide a mechanistic foundation for the experimental performance decay of MIL-125 in photocatalytic nitrate reduction, explicitly linking the increased energy barrier for the rate-determining step to the observed kinetic slowdown. For isolated Ti^{3+} sites, the rate-determining step is NH_3 desorption with a barrier of 3.17 eV, whereas agglomerated sites shift the bottleneck to *N formation from *NOH with a higher barrier of 3.59 eV, as depicted in Fig. 5d. This computational barrier increase directly correlates with the experimental decline in NH_4^+ production rate from 738.32 to 612.82 μmol g^{-1} h^{-1} over recycling cycles, shown in Fig. 2e, where Ti^{3+} site aggregation impedes charge separation and elevates the kinetic hurdle. Thus, the synergy between DFT and experimental data solidifies that preserving isolated Ti^{3+} sites is crucial to maintain low energy barriers and high efficiency.

4 Conclusions

In conclusion, we demonstrate that the photocatalytic efficiency of MIL-125 for nitrate reduction to ammonia is critically governed by the atomic dispersion of Ti^{3+} sites within its structure. The as-synthesized catalyst, featuring isolated Ti^{3+} sites, achieves a high NH_3 production rate of 738.32 μmol g^{-1} h^{-1} by facilitating strong nitrate adsorption and providing photo-generated electrons with high reduction potential. However, prolonged photoreaction induces increased loss of organic linkers, leading to the formation of agglomerated Ti^{3+} sites. This transformation detrimentally alters the catalyst's properties, causing a positive shift in the conduction band that reduces electron reducibility, impairing charge separation efficiency, and increasing the energy barrier of the rate-determining step. Consequently, the agglomerated Ti^{3+} sites result in a significant decline in photocatalytic activity. These findings reveal that the initial high performance is intrinsically linked to the presence of isolated Ti^{3+} sites, while the subsequent deactivation is a direct result of their aggregation under operating conditions. Therefore, the long-term stability and efficiency of MIL-125-based photocatalysts depend on developing strategies to mitigate linker deficiency and preserve the atomic dispersion of active metal sites, highlighting a crucial design principle for durable MOF photocatalysts in sustainable nitrogen cycling applications.

Author contributions

L. L., R. S. and R. Y. contributed to the conception and design of the experiments. L. L. directed the project and analyzed the data. L. L. and G. Z. performed the experiments and analyzed the data. L. L. wrote the manuscript. X. W. and J. Z. provided valuable suggestions during the project. All authors discussed the results and commented on the manuscript.

Conflicts of interest

There are no conflicts to declare.

Data availability

The data supporting this article have been included as part of the supplementary information (SI).

Supplementary information: characterization and experimental details, DFT calculations details, comparison of the photocatalytic ammonia synthesis efficiency between MIL-125 in this work and recently reported photocatalysts, and Mott–Schottky curves of MIL-125 after a 1 h photocatalytic nitrate reduction reaction. See DOI: https://doi.org/10.1039/d5sc09647b.

Acknowledgements

We gratefully acknowledge the support of the Scientific Research Foundation for High-level Talents of Anhui University of Science and Technology (No. 2025yjrc0125), the State Key Laboratory of Heavy Oil Processing, China University of Petroleum (No. SKLHOP202402009), the Shandong Provincial Natural Science Foundation (No. ZR2023QD036), the Hubei Key Laboratory of Novel Reactor and Green Chemical Technology (No. NRG202506), and the State Key Laboratory of New Textile Materials and Advanced Processing, Wuhan Textile University (No. FZ2025028).

Notes and references

1 G. Youn, I. Hong, B. Song, D. Lee, Y. Yun, H. S. Moon and K. Yong, *Sol. RRL*, 2024, **8**, 2300880.
2 X. He, J. Li, R. Li, D. Zhao, L. Zhang, X. Ji, X. Fan, J. Chen, Y. Wang, Y. Luo, D. Zheng, L. Xie, S. Sun, Z. Cai, Q. Liu, K. Ma and X. Sun, *Inorg. Chem.*, 2023, **62**, 25–29.
3 H. S. Moon, B. Song, J. Jeon, T.-H. Lai, Y.-P. Chang, Y.-D. Lin, J. K. Park, Y.-G. Lin, Y.-J. Hsu, H. Shin, Y. Yun and K. Yong, *Appl. Catal., B*, 2023, **339**, 123185.
4 K. Fan, W. Xie, J. Li, Y. Sun, P. Xu, Y. Tang, Z. Li and M. Shao, *Nat. Commun.*, 2022, **13**, 7958.
5 J. Li, R. Chen, J. Wang, Y. Zhou, G. Yang and F. Dong, *Nat. Commun.*, 2022, **13**, 1098.
6 H. Hirakawa, M. Hashimoto, Y. Shiraishi and T. Hirai, *ACS Catal.*, 2017, **7**, 3713–3720.
7 S. Yin, Z. Guan, Y. Zhu, D. Guo, X. a. Chen and S. Wang, *ACS Nano*, 2024, **18**, 27833–27852.
8 L. Wei, Y. Zhang, C. Zhang, C. Yao, C. Ni and X. Li, *ACS Appl. Nano Mater.*, 2023, **6**, 13127–13136.
9 S. Han, H. Li, T. Li, F. Chen, R. Yang, Y. Yu and B. Zhang, *Nat. Catal.*, 2023, **6**, 402–414.
10 A. P. Varghese and S. K. Lakhera, *Renewable Sustainable Energy Rev.*, 2024, **200**, 114537.

11 I. Hong, H. S. Moon, B. J. Park, Y.-A. Chen, Y.-P. Chang, B. Song, D. Lee, Y. Yun, Y.-J. Hsu, J. W. Han and K. Yong, *Chem. Eng. J.*, 2024, **484**, 149506.
12 Z. Liu, S. Fan, X. Li, Z. Niu, J. Wang, C. Bai, J. Duan, M. O. Tadé and S. Liu, *Appl. Catal., B*, 2023, **327**, 122416.
13 Y. Wang, H. Yin, X. Zhao, Y. Qu, A. Zheng, H. Zhou, W. Fang and J. Li, *Appl. Catal., B*, 2024, **341**, 123266.
14 H. Jung, G. Cha, H. Kim, J. Will, X. Zhou, E. Spiecker, J. Breu and P. Schmuki, *J. Am. Chem. Soc.*, 2025, **147**, 9049–9055.
15 A. P. Varghese, R. T. P, B. Neppolian, A. S. AlArifi and S. K. Lakhera, *ACS Appl. Energy Mater.*, 2024, **7**, 6527–6536.
16 C. Zhang, Y. Wu, D. Li and H.-L. Jiang, *Chem. Sci.*, 2025, **16**, 13149–13172.
17 T. Wang, Y. Wang, M. Sun, A. Hanif, H. Wu, Q. Gu, Y. S. Ok, D. C. W. Tsang, J. Li, J. Yu and J. Shang, *Chem. Sci.*, 2020, **11**, 6670–6681.
18 Y. Yao, X. Wei, H. Zhou, K. Wei, B. Kui, F. Wu, L. Chen, W. Wang, F. Dai, P. Gao, N. Wang and W. Ye, *ACS Catal.*, 2024, **14**, 16205–16213.
19 Y. Zhao, J. Shen, J. Yuan, H. Mao, X. Cheng, Z. Xu and Z. Bian, *Nano Energy*, 2024, 109499.
20 Y. Xi, Y. Xiang, T. Bao, Z. Li, C. Zhang, L. Yuan, J. Li, Y. Bi, C. Yu and C. Liu, *Angew. Chem., Int. Ed.*, 2024, **63**, e202409163.
21 J. Deng, X. Hu, A. J. Klaver, J. Liu, B. Liu, L. Bai, M. Xie and D. Zhang, *Chem. Rev.*, 2025, **125**, 11260–11357.
22 S. C. Moore, M. R. Smith, J. L. Trettin, R. A. Yang and M. L. Sarazen, *ACS Energy Lett.*, 2023, **8**, 1397–1407.
23 W. R. Heinz, I. Agirrezabal-Telleria, R. Junk, J. Berger, J. Wang, D. I. Sharapa, M. Gil-Calvo, I. Luz, M. Soukri, F. Studt, Y. Wang, C. Wöll, H. Bunzen, M. Drees and R. A. Fischer, *ACS Appl. Mater. Interfaces*, 2020, **12**, 40635–40647.
24 C.-D. Hao, Z.-Y. Zhang, A.-X. Yu, J.-J. Li, Q. Liu, X.-J. Bo, D.-Y. Du, S. Yuan and Z.-M. Su, *Inorg. Chem.*, 2025, **64**, 10001–10011.
25 C. Fan, V. Nguyen, Y. Zeng, P. Phadungbut, T. Horikawa, D. D. Do and D. Nicholson, *Microporous Mesoporous Mater.*, 2015, **209**, 79–89.
26 Y. Sun, H. Ji, Y. Sun, G. Zhang, H. Zhou, S. Cao, S. Liu, L. Zhang, W. Li, X. Zhu and H. Pang, *Angew. Chem., Int. Ed.*, 2024, **63**, e202316973.
27 L. Hu, W. Wu, L. Gong, H. Zhu, L. Jiang, M. Hu, D. Lin and K. Yang, *Angew. Chem., Int. Ed.*, 2023, **62**, e202215296.
28 Q. Zhang, Y. Chen, X. Yu, Y. Yin, Y. Ru and G. Tian, *Catal. Sci. Technol.*, 2023, **13**, 4525–4533.
29 X. Song, Y. Wang, T. Zhu, J. Liu and S. Zhang, *Chem. Eng. J.*, 2021, **416**, 129126.
30 C. Liu, Q. Chen, Y. Chen, J. C. Yu, J. Wu and L. Wu, *J. Colloid Interface Sci.*, 2025, **678**, 616–626.
31 L. Liu, Z. Chen, J. Wang, D. Zhang, Y. Zhu, S. Ling, K.-W. Huang, Y. Belmabkhout, K. Adil, Y. Zhang, B. Slater, M. Eddaoudi and Y. Han, *Nat. Chem.*, 2019, **11**, 622–628.
32 X. Sun, L. Sun, G. Li, Y. Tuo, C. Ye, J. Yang, J. Low, X. Yu, J. H. Bitter, Y. Lei, D. Wang and Y. Li, *Angew. Chem., Int. Ed.*, 2022, **61**, e202207677.
33 M. Shi, Z. Liu, S. Zhang, S. Liang, Y. Jiang, H. Bai, Z. Jiang, J. Chang, J. Feng, W. Chen, H. Yu, S. Liu, T. Wei and Z. Fan, *Adv. Energy Mater.*, 2022, **12**, 2103657.
34 C. An, A. Sikandaier, X. Guo, Y. Zhu, H. Tang and D. Yang, *Acta Phys.-Chim. Sin.*, 2024, **40**, 2405019.
35 L. Ni, Y. Xiao, X. Zhou, Y. Jiang, Y. Liu, W. Zhang, J. Zhang and Z. Liu, *Inorg. Chem.*, 2022, **61**, 19552–19566.
36 P. H. M. Andrade, H. Ahouari, C. Volkringer, T. Loiseau, H. Vezin, M. Hureau and A. Moissette, *ACS Appl. Mater. Interfaces*, 2023, **15**, 31032–31048.
37 G.-Y. Han, Y. Ji, X.-Y. Li, Y. Gai, G.-Z. Hou, Q.-Y. Cheng, Z. Zhang, Y. Liu, J. Wang, P. Van Der Voort, G. Hou, X.-P. Wu, G. He and X. Feng, *Adv. Sci.*, 2025, **12**, e10578.